

Multiscale Analysis for Field-Effect Penetration through Two-Dimensional Materials

Tian Tian,[†] Peter Rice,^{‡,¶} Elton J. G. Santos,^{*,‡,¶} and Chih-Jen Shih^{*,†}

[†]*Institute for Chemical and Bioengineering, ETH Zürich, Zürich 8093, Switzerland*

[‡]*School of Mathematics and Physics, Queen’s University Belfast, United Kingdom*

[¶]*School of Chemistry and Chemical Engineering, Queen’s University Belfast, United Kingdom*

E-mail: e.santos@qub.ac.uk; chih-jen.shih@chem.ethz.ch

Abstract

Gate-tunable two-dimensional (2D) materials-based quantum capacitors (QCs) and van der Waals heterostructures involve tuning transport or optoelectronic characteristics by the field effect. Recent studies have attributed the observed gate-tunable characteristics to the change of the Fermi level in the first 2D layer adjacent to the dielectrics, while the penetration of the field effect through the one-molecule-thick material is often ignored or over-simplified. Here, we present a multiscale theoretical approach that combines first-principles electronic structure calculations and the Poisson-Boltzmann equation methods to model penetration of the field effect through graphene in a metal-oxide-graphene-semiconductor (MOGS) QC, including quantifying the degree of “transparency” for graphene two-dimensional electron gas (2DEG) to an electric displacement field. We find that the space charge density in the semiconductor layer can be modulated by gating in a nonlinear manner, forming an accumulation or

inversion layer at the semiconductor/graphene interface. The degree of transparency is determined by the combined effect of graphene quantum capacitance and the semiconductor capacitance, which allows us to predict the ranking for a variety of monolayer 2D materials according to their transparency to an electric displacement field as follows: graphene > silicene > germanene > WS₂ > WTe₂ > WSe₂ > MoS₂ > phosphorene > MoSe₂ > MoTe₂, when the majority carrier is electron. Our findings reveal a general picture of operation modes and design rules for the 2D-materials-based QCs.

Keywords

Graphene, quantum capacitance, field effect, two-dimensional materials, ab initio calculations, transition metal dichalcogenides

The field effect refers to the modulation of the space charge concentration in a semiconductor by applying an electric displacement field.¹ Over the past few decades, this effect has been utilized to enable a wide range of metal-oxide-semiconductor (MOS) electronics, including the field-effect transistors (FETs) and the floating-gate memory devices.¹ On the other hand, the two-terminal active electronic components, such as diodes, which consist of semiconductor layers sandwiched between two metallic electrodes, fundamentally prohibit introduction of the field effect due to strong electric-field screening in metal.² In 1988, Luryi proposed the concept of “quantum capacitors (QCs)” and discussed the possibility of using two-dimensional electron gas (2DEG) as one terminal that allows partial penetration of the field effect.³ The 2DEG was subsequently realized by trapping electrons in a quantum well⁴ or confining an inversion layer in a metal-oxide-semiconductor (MOS) capacitor.¹ However, despite great success in demonstration of concept, the 2DEGs are limited in a few materials systems and often require complicated device architecture.⁵

Graphene, a zero-bandgap semimetal consisting of a two-dimensional, atomically-thin lattice of sp^2 -bonded carbon atoms,⁶ combines high carrier mobility⁷ and Fermi-energy tunability.^{8–10} Recent development in other two-dimensional semimetals and semiconductors, such as silicene,¹¹ germanene,¹² phosphorene (monolayer black phosphorus)^{13,14} and monolayer transition metal dichalcogenides (TMDs),¹⁵ has further suggested new opportunities in integrating them into different materials systems. Due to the fact that the thickness of these one-molecule-thick materials is comparable to their Debye screening length, they have been considered as the ideal candidates of 2DEG¹⁶ to realize the QC devices on a large scale. Very recently, the idea of using graphene 2DEG as one terminal to modulate the characteristics of the two-terminal electronic device via gating has been utilized in many graphene-based vertical electronics and van der Waals (vdW) heterostructures,¹⁷ including vertical transistors (or barristors),^{18–21} solar cells^{22–24} and light emitting diodes.²⁵ Indeed, most of these devices can be categorized as QCs at some extension. Nevertheless, most reports have attributed the observed gate-tunable transport behavior to the change of graphene’s work function,

while the penetration of the field effect through graphene 2DEG, as well as the effect of the diode bias, are often ignored or over-simplified. A more complete theoretical picture and analysis are required to elucidate the graphene-based QCs in terms of the interplay between the penetration of field effect and the electronic structure of the 2D materials.

In this letter, we present a mutiscale theoretical approach to model the space charge distribution in a metal-oxide-graphene-semiconductor (MOGS) QC giving a quantitative interpretation of the field-effect penetration into the device. From both macroscopic modeling using Poisson-Boltzmann equation methods and first-principles *ab initio* calculations at different levels of accuracy, we find that the space charge density in the semiconductor layer can be modulated by the field effect through the graphene layer, thereby creating an accumulation or inversion layer at the graphene-semiconductor interface. Accordingly, the degree of “transparency” of the graphene 2DEG to an electric displacement field is quantified and proven to be as a result of the combined effect of the graphene quantum capacitance, C_G , and the semiconductor capacitance, C_S . By combining with the density functional theory (DFT) calculations, we have used the obtained analytical relations to rank a variety of 2D (e.g. silicene, germanene, phosphorene and TMDs) materials according to their transparency to an electric displacement field. Finally, the effect of the bias voltage applied on the semiconductor terminal, V_b is discussed. Our analysis show that because the semiconductor capacitance increases significantly with V_b , the penetration of the field effect in a MOGS QC becomes much less effective beyond a certain V_b range which can guide to optimum design functioning rules.

Figure 1a shows an one-dimensional MOGS system comprised of a metal (M) electrode, a dielectric oxide (O) layer, a sheet of undoped monolayer graphene (G), and a bulk semiconductor (S) layer with the thickness d_S . A gate voltage V_M is applied between the metal and graphene terminals to electrostatically induce space charges in graphene and the semiconductor layer. An ohmic contact is used on the semiconductor side to apply bias voltage V_b between the semiconductor and graphene terminals.

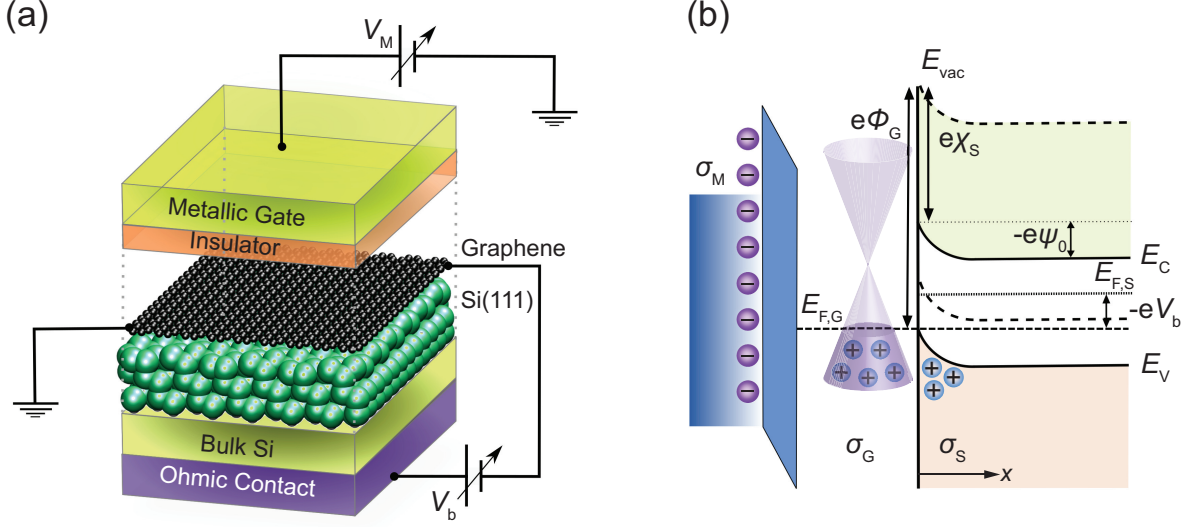


Figure 1: (a) Schematic illustration for the setup of a MOGS QC. (b) Schematic band diagram of a MOGS QC.

First, the electroneutrality of the entire system suggests:

$$\sigma_M + \sigma_G + \sigma_S = 0 \quad (1)$$

where σ_M and σ_G and σ_S are the surface charge density in the metal, graphene, and semiconductor terminals, respectively. The x coordinate is defined as the distance away from the semiconductor/graphene (SG) interface in the semiconductor layer. According to the Gauss's law, σ_S is given by:

$$\sigma_S = \int_0^{d_S} \rho(x) dx = -\epsilon_S \mathcal{E}_0 \quad (2)$$

where $\rho(x)$ is the space charge density at position x in semiconductor; ϵ_S is the dielectric constant of semiconductor, and \mathcal{E}_0 is the electric field at the SG interface. We assume that the electric potential in the semiconductor layer, $\psi(x)$, satisfies the Poisson-Boltzmann equation:

$$\frac{d^2\psi(x)}{dx^2} = -\frac{e\rho(x)}{\epsilon_S} = -\frac{e}{\epsilon_S} [p_0(e^{-\beta\psi(x)} - 1) - n_0(e^{\beta\psi(x)} - 1)] \quad (3)$$

where e is the elementary charge, $\beta = e/k_B T$, k_B is the Boltzmann constant, T is tem-

perature and n_0 , p_0 are the equilibrium densities of electron and hole in bulk semiconductor, respectively. Considering the limit that the Debye length in the semiconductor layer $\lambda_D \approx \sqrt{\frac{\epsilon_S k_B T}{e^2 N_D}}$ (where N_D is the dopant density) is much smaller than d_S , the boundary conditions $\psi(0) = \psi_0$, $\psi(\infty) = 0$ and $\psi'(\infty) = 0$ are used for eq 3, where ψ_0 is the electric potential at the SG interface. By integrating eq 3 with respect to x , one can determine the semiconductor space charge density σ_S as a function of ψ_0 as follows:

$$\sigma_S(\psi_0) = -\epsilon_S \text{sign}(\psi_0) \sqrt{\frac{2e}{\beta \epsilon_S}} \sqrt{p_0(e^{-\beta \psi_0} + \beta \psi_0 - 1) + n_0(e^{\beta \psi_0} - \beta \psi_0 - 1)} \quad (4)$$

In order to determine the electric potential at the SG interface, ψ_0 , the Schottky-Mott rule, which assumes that the vacuum levels for graphene and semiconductor at the interface are aligned, is employed. Note that this assumption holds when the interface states at the SG interface are negligible.^{26,27} It follows that:

$$\psi_0 = \frac{E_{C,\infty} - E_{F,\infty}}{e} - \phi_G + \chi_S - V_b \quad (5)$$

where $E_{C,\infty}$ and $E_{F,\infty}$ are the conduction-band and Fermi levels in semiconductor at the flat-band condition, and χ_S is the electron affinity of the semiconductor layer (see Figure 1b). ϕ_G is the work function of graphene as a function of σ_G , which is assumed to follow the elementary electronic properties of graphene,²⁸ without considering the electron-hole puddles induced by the surroundings:²⁹

$$\phi_G = \phi_G^0 + \text{sign}(\sigma_G) \frac{\hbar v_F}{e} \sqrt{\frac{\pi |\sigma_G|}{e}} \quad (6)$$

where \hbar is the reduced Planck constant, $v_F \approx 1.1 \times 10^6 \text{ m}\cdot\text{s}^{-1}$ is the Fermi velocity in graphene and $\phi_G^0 = 4.6 \text{ V}$ is the work function of graphene at the charge neutrality point (CNP) corresponding to $\sigma_G = 0$.¹⁰ Note that a nonzero quantum capacitance of graphene, $C_G = \partial \sigma_G / \partial \phi_G$, the application of V_M to the MOGS QC considered here (Figure 1a) includes

the shift in the work function of graphene, or namely,

$$V_M = \frac{\sigma_M}{C_{\text{ox}}} + \int_{\sigma_G|V_M=0}^{\sigma_G} \frac{1}{C_G} d\sigma_G \quad (7)$$

where C_{ox} is the capacitance of the dielectric oxide layer. It suggests that at $V_M = 0$, ϕ_G does not necessarily coincide with the CNP, depending on the doping level of the adjacent semiconductor layer. By using eqs 1 and 4-6, the electric potential at the SG interface, ψ_0 , as a function of σ_M , can be determined analytically. Subsequently, by using the boundary conditions of $\psi(0) = \psi_0$ and $\psi_0 = \sigma_S/\epsilon_S$ in eq 3 the $\psi(x)$ profile is solved numerically, allowing us to construct the associated band diagrams.

Here we consider a doped silicon layer in the MOGS QC structure at room temperature (300 K), where $\chi_S = 4.0$ V, the bandgap $E_g = 1.12$ eV, the relative dielectric constant $\epsilon_r = 11.8$ and the intrinsic carrier concentration $n_i = 9.7 \times 10^9 \text{ cm}^{-3}$.³⁰ First we analyze the case of free contact between the graphene and the semiconductor layers, i.e., $\sigma_G + \sigma_S = 0$ and $V_M = V_b = 0$. Figure 2a presents the change of Fermi level in graphene, $\Delta E_{F,G} = -(\phi_G - \phi_G^0)$, as a function of the electron concentration at equilibrium n_0 . Note that when $n_0 < n_i$, the majority carriers are holes, or the semiconductor is p-doped. Indeed, in order to fulfill the Schottky-Mott rule, the work function difference across the SG interface results in a charge transfer at the interface. A nearly symmetric response of $\Delta E_{F,G}$ with respect to the silicon doping level reflects the fact that the work function of intrinsic silicon, $\phi_S^0 = 4.56$ V, is very close to ϕ_G^0 . When the silicon layer is heavily doped ($> 10^{15} \text{ cm}^{-3}$ for the majority carrier), a relatively pronounced transfer of majority carrier occurs, with a $\Delta E_{F,G}$ up to ± 0.2 eV.

Next, we apply a nonzero σ_M to the metal terminal, corresponding to a V_M described by eq 7. A proper range of σ_M up to $\pm 2 \times 10^{13} \text{ e} \cdot \text{cm}^{-2}$, which can be reached by using a high-k dielectric oxide layer.⁹ σ_M and σ_S are subsequently altered as a result of the field effect. The $\Delta E_{F,G} - \sigma_M$ curves at different silicon doping levels are shown in Figure 2b. By solving eq 6 with $\sigma_G + \sigma_M = 0$, the curve associated with a MOG QC is also shown for comparison. As

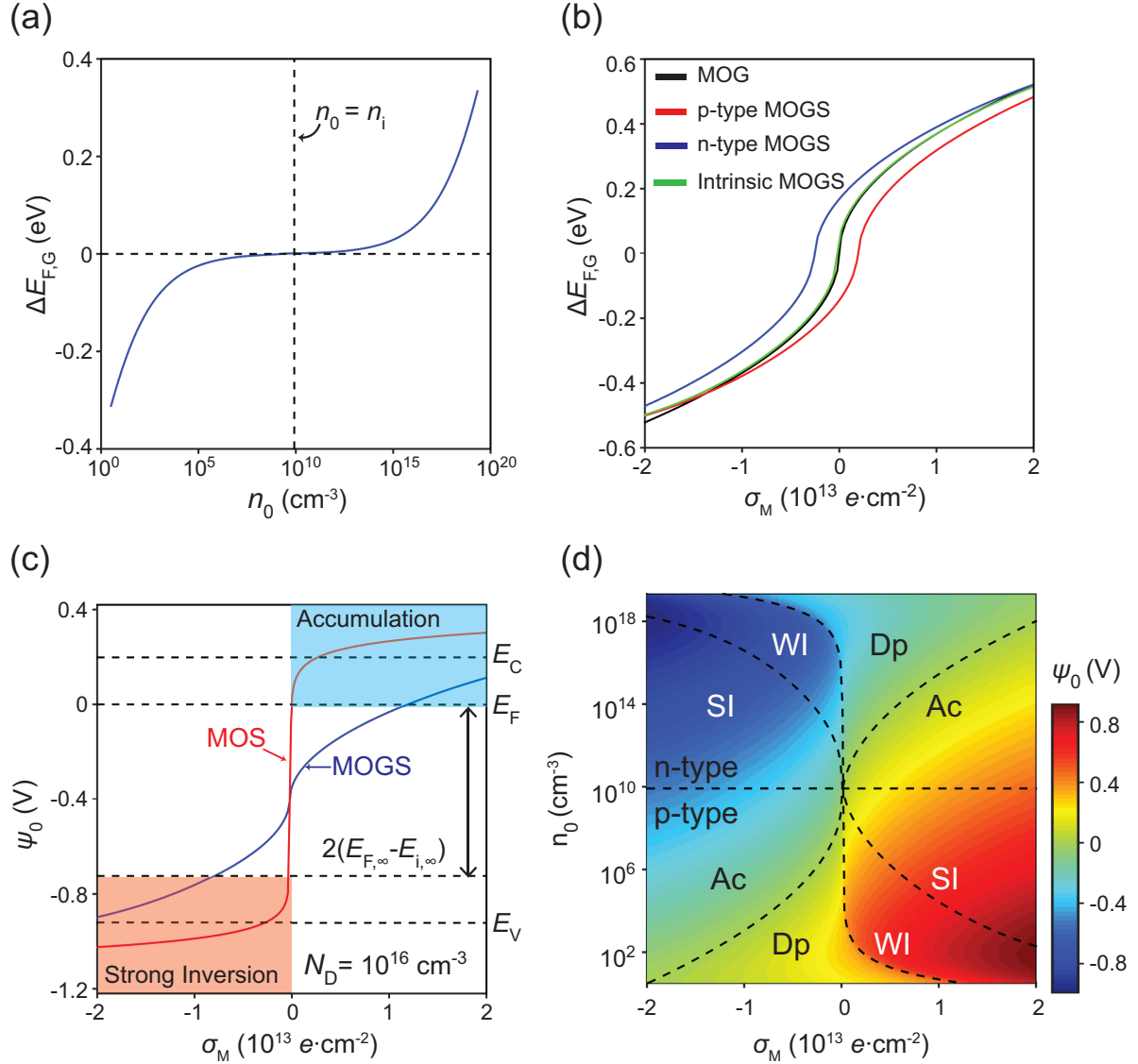


Figure 2: (a) The calculated Fermi level change of graphene, $\Delta E_{F,G}$, as a function of n_0 in Si when considering free contact between the graphene and Si layers. (b) The calculated $\Delta E_{F,G}$ as a function of σ_M in a MOG capacitor and a MOGS QC. The doping level of majority carrier in p-type/n-type Si is 10^{18} cm^{-3} . (c) The calculated ψ_0 as a function of σ_M in n-type ($N_D = 10^{16} \text{ cm}^{-3}$) MOS and MOGS capacitors. The accumulation (light blue) and strong inversion (pink) regimes are also shown for comparison. (d) The calculated contour map of ψ_0 as a function of σ_M and n_0 . The accumulation (Ac), depletion (Dp), weak inversion (WI), and strong inversion (SI) regimes are defined accordingly.

well-stated in literature,³¹ due to a small density of states (DOS) near the CNP of graphene, $\Delta E_{F,G}$ changes rapidly as $\sigma_M \rightarrow 0$ in the MOG QC. In the range of σ_M considered, one can tune the Fermi level of graphene up to ± 0.5 eV. On the other hand, regarding the MOGS QCs in which graphene is in contact with a silicon layer, when an intrinsic Si is used, we do not find a notable difference until a relatively high $|\sigma_M|$ is applied. Nevertheless, when the Si layer is heavily doped (with a majority dopant concentration of 10^{18} cm^{-3}), an considerable deviation from the $\Delta E_{F,G} - \sigma_M$ curve of MOG is observed. It suggests that $\sigma_G + \sigma_M$ (which is equal to $-\sigma_S$ numerically) becomes nonzero, or in other words, the induced charges in graphene partially “leak” to the adjacent semiconductor layer. We therefore suggest that the estimation of graphene’s work function using $\phi_G|_{\sigma_G=-\sigma_M}$ in a MOGS QC, as has been widely used to estimate the work function of graphene in a MOGS QC (e.g. ref. 20) appears to be incorrect. Indeed, in a MOGS QC, graphene behaves like a 2DEG and is not capable of completely screening the electric displacement field applied.

In order to further understand the penetration of the field effect through graphene, Figure 2c compares the evolutions of calculated ψ_0 with σ_M in a standard metal-oxide-semiconductor (MOS) capacitor and a MOGS QC ($N_D = 10^{16} \text{ cm}^{-2}$), as a function of σ_M . In a standard MOS capacitor, the field effect allows to modulate the space charge concentration in the semiconductor layer significantly by applying a relatively small σ_M , such that ψ_0 changes rapidly and moves beyond the conduction and valence band energy levels (E_C and E_V). On the other hand, in a MOGS QC, the modulation of ψ_0 is observed to be less sensitive to σ_M , suggesting that the field effect only partially penetrates through graphene. Nevertheless, one can still tune ψ_0 from the strong inversion regime (pink, corresponding to $p(x=0) > N_D$) to the accumulation regime (light blue, corresponding to $n(x=0) > N_D$), but not to the band edges. Clearly, unlike the standard MOS capacitors, we predict that the MOGS QC devices inherently do not facilitate fast switching by the field effect.

Another important observation in Figure 2b is that σ_G also depends on the doping level of the adjacent Si layer. In order to further discuss this effect, Figure 2d presents the contour

map of ψ_0 as functions of σ_M and n_0 . We also include three curves associated with: (i) $\psi_0 = 0$, (ii) $\psi_0 = -(E_{F,\infty} - E_{i,\infty})/e$, and (iii) $\psi_0 = -2(E_{F,\infty} - E_{i,\infty})/e$, where $E_{i,\infty}$ is the intrinsic energy level of semiconductor at the flat-band condition. Note that the three curves intersect at (n_i, σ_M^0) , in which σ_M^0 is given by

$$\sigma_M^0 = \text{sign}(\phi_G^0 - \phi_S^0) \frac{(\phi_G^0 - \phi_S^0)^2 e^3}{\pi \hbar^2 v_F^2} \quad (8)$$

where ϕ_S^0 is the work function of intrinsic semiconductor. Following the convention in semiconductor physics,¹ the three curves divide the contour map into four regimes as follows: (i) the accumulation (Ac), (ii) the depletion (Dp), (iii) the weak inversion (WI), and (iv) the strong inversion (SI). As shown, within the σ_M range considered, the partially-penetrated field effect allows the induction of an inversion or accumulation layer at the SG interface, unless the semiconductor doping level is relatively high (with an majority carrier concentration $> 10^{18} \text{ cm}^{-3}$). The wide tunability results from the following two facts: (i) σ_S^0 is very close to σ_G^0 , and (ii) the bandgap is comparable to the tunable range of $E_{F,G}$. Our findings explain why Si has been considered as a good semiconductor candidate in the MOGS QCs.^{18,24}

Based on the above analysis, we propose and derive an expression for the index η that quantifies the degree of transparency to an electric displacement field in a MOGS QC as follows:

$$\eta = -\left(\frac{\partial \sigma_S}{\partial \sigma_M}\right) \quad (9)$$

We can deduce that $-(\partial \sigma_G / \partial \sigma_M) = 1 - \eta$, and by taking that (i) $(\partial \phi_G / \partial \psi_S) = -1$ (see eq 5), (ii) the quantum capacitance of graphene $C_G = \partial \sigma_G / \partial \phi_G$ and (iii) the capacitance of semiconductor $C_S = -(\partial \sigma_S / \partial \psi_0)$, the transparency index η in eq 9 can be decomposed

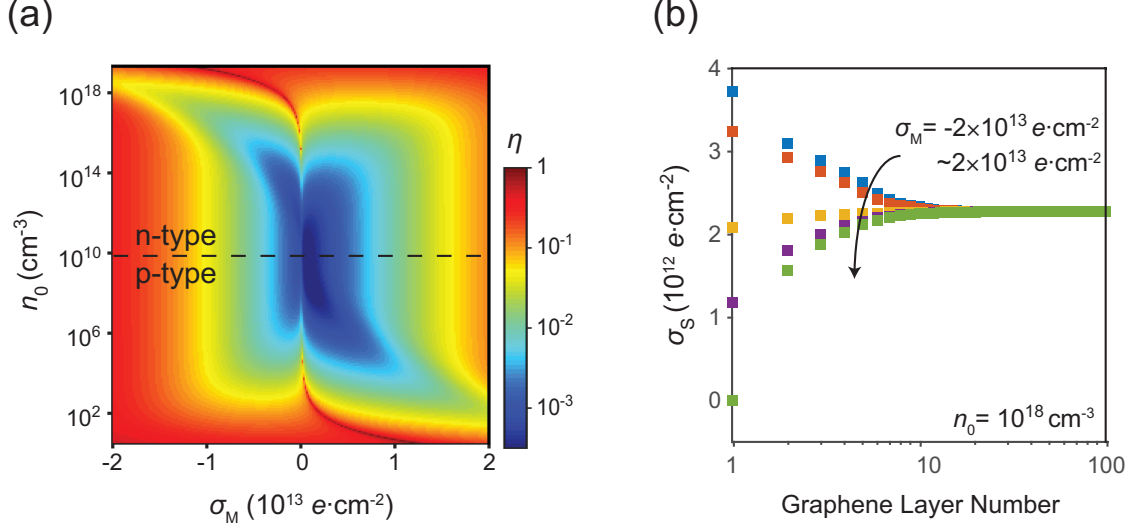


Figure 3: (a) Calculated transparency of graphene 2DEG to electric displacement field in a MOGS QC, as functions of σ_M and n_0 . (b) Calculated σ_S as a function of number of graphene layers in a MOGS QC ($n_0 = 10^{18} \text{ cm}^{-3}$). The arrow indicates the direction of increasing σ_M .

using the chain rule and follows

$$\begin{aligned} \eta &= \left(\frac{\partial \sigma_S}{\partial \psi_0} \right) \left(\frac{\partial \sigma_G}{\partial \phi_G} \right)^{-1} \left(\frac{\partial \sigma_G}{\partial \sigma_M} \right) \\ &= \frac{1}{1 + C_G/C_S} = \left(1 + \frac{2}{\hbar v_F} \sqrt{\frac{e^3 |\sigma_G|}{\pi}} \frac{\mathcal{E}_0}{\rho_0} \right)^{-1} \end{aligned} \quad (10)$$

where ρ_0 is the charge density at the SG interface. We also consider the effect of interface states on the transparency of graphene (see Supporting Information), which suggests that the existence of an interfacial layer reduces the transparency. In practice, although the interface states are difficult to be removed completely, their influence can be minimized by creating a clean semiconductor surface with minimal interfacial contamination.²⁵ Thereafter we still use the expression of eq 10 to simplify the following analysis.

Accordingly, the contour map of η as a function of σ_M and n_0 is shown in Figure 3a. Eq 10 suggests that the transparency of graphene 2DEG to an electric displacement field is determined by the combined effects of the graphene quantum capacitance and the semiconductor capacitance. As a result, the limit of perfect transparency, $\eta \rightarrow 1$, occurs when $C_G \rightarrow 0$, corresponding to the CNP of graphene, along the curve of $\psi_0 = 0$ in Figure 2d. However, we

observe that this transparency disappears by slightly changing σ_M , due to the rapid increase of ϕ_G with σ_G near the CNP of graphene.³¹ In practice, considering the residual charges induced by the electron-hole puddles near the CNP of graphene,²⁹ we predict that the limit of $\eta \rightarrow 1$ may not be observable experimentally. On the other hand, a general trend exhibited in Figure 3a is that one can gain a higher degree of transparency for the graphene 2DEG by: (i) increasing the doping level in the Si layer, and (ii) applying a higher $|\sigma_M|$, resulting a considerable increase of C_S . We can further conclude from eq 10 that when the graphene layer number increases, the field-effect transparency would be attenuated. Intuitively speaking, the total DOS of multilayer graphene increases with the layer number and results in a larger C_G value. In the case of graphite with infinite layers of graphene, the electric displacement field is completely screened and σ_S becomes independent of σ_M . Here, instead of deriving the total DOS of multilayer graphene by the tight-binding model³² or *ab initio* calculations, we propose a simplified model, which assumes that the interlayer coupling is negligible and each layer behaves as monolayer graphene (see details in Supporting Information). The σ_S calculated under different σ_M as a function of graphene layer number are shown in Figure 3b. We observe that σ_S becomes independent of σ_M when more than 10 layers of graphene are used in the MOGS QC, and consequently, the transparency decays to nearly zero with graphene layer number (Supporting Information Figure S5). This is in agreement with the non-linear nature of the screening in multilayer graphene,³³ which shows a high polarization charge at a few graphene layers adjacent to an external electric displacement field, while the charge in graphene decays exponentially in deeper layers.

The above analysis based on Poisson-Boltzmann equation methods is still valid at different levels of theory as calculated using first-principles methods within density functional theory (DFT) including van der Waals interactions (see *Methods* for details). Figure 4 shows the calculated electronic response on a graphene/Si(111) interface considering the effect of σ_M . We find that, irrespective of the doping levels considered, both σ_G and σ_S monotonically decrease as σ_M increases (Fig. 4a and b). Similar to Figure 2b, the amount of induced

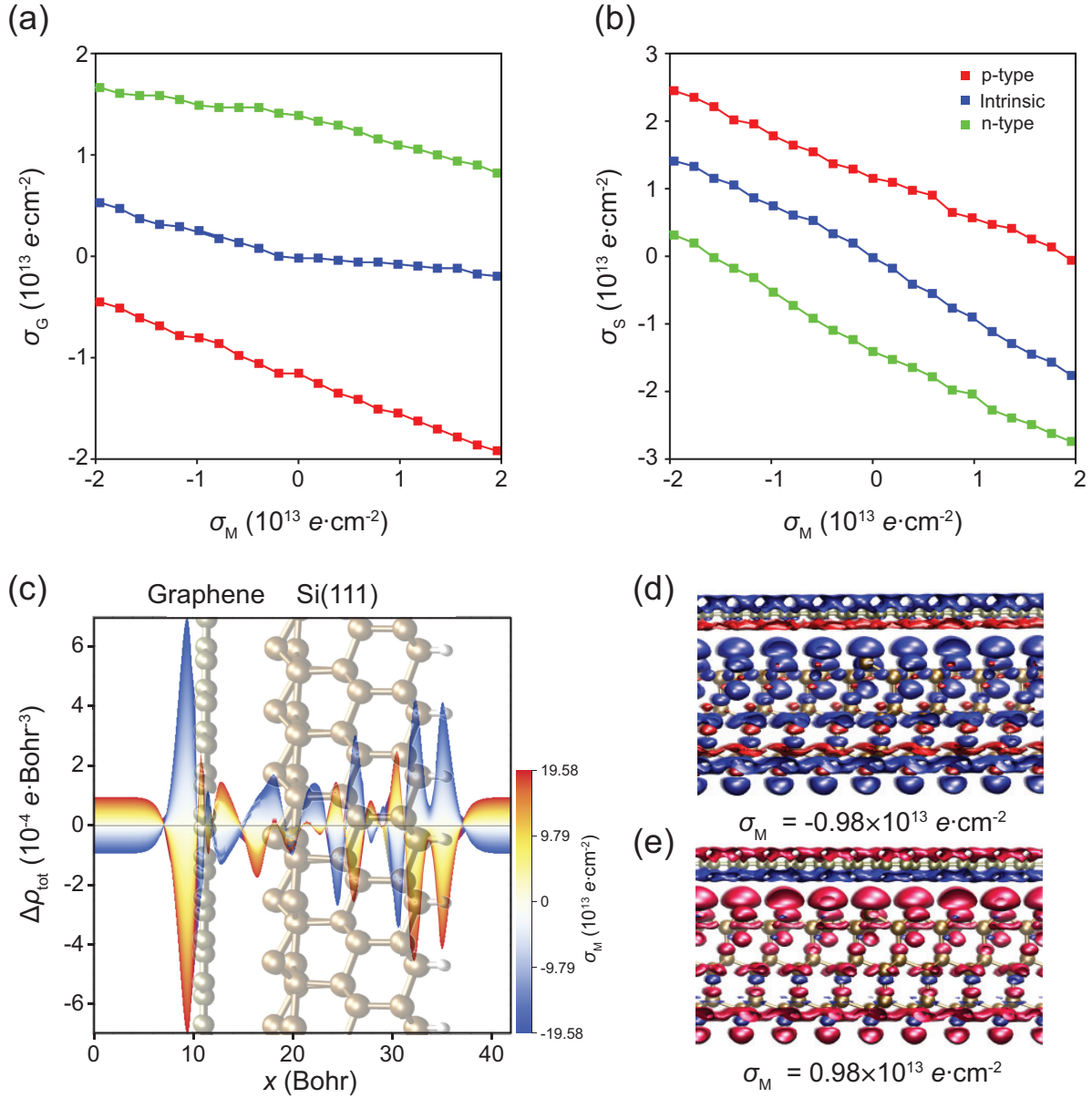


Figure 4: Induced charge densities at (a) graphene, σ_G , and (b) Si(111), σ_S , as a function of σ_M in different systems: intrinsic (blue), p-type (green) and n-type (red) Si, respectively. The average carrier numbers per unit area in the whole Si slab are $1.10 \times 10^{13} \text{ cm}^{-2}$ for p-type Si and $-1.10 \times 10^{13} \text{ cm}^{-2}$ for n-type Si. (c) Total average charge density cross section $\Delta\rho_{\text{tot}}$ as a function of the coordinate x perpendicular to the graphene/Si(111) interface. The positions of graphene and Si(111) are marked with the underneath faint structure. The color gradient shows the evolution of σ_M as displayed on the right side. Molecular visualizations of the induced charge density in graphene and intrinsic Si layers (cutoff at $\pm 0.0021 \text{ e}\cdot\text{Bohr}^{-3}$) when (d) $\sigma_M = -0.98 \times 10^{13} \text{ cm}^{-2}$ and (e) $\sigma_M = 0.98 \times 10^{13} \text{ cm}^{-2}$. Blue and red isosurfaces represent positive and negative charges, respectively.

charges in both graphene and Si layers as a result of σ_M can be deviated by different doping levels of Si. These results indicate that the graphene 2DEG is also transparent to the electric displacement field from the first-principles calculations. We also observe that both σ_G and σ_S show a nearly linear relation with σ_M when very high σ_M (up to $\pm 20 \times 10^{13} \text{ e}\cdot\text{cm}^{-2}$) is applied (Supporting Information Figure S1), which allows us to extract the η by performing a linear-fitting to the $\sigma_S - \sigma_M$ curves using the formula $\sigma_S = -\eta\sigma_M + b$, where b is a constant. Interestingly, regardless of the Si doping level, all three systems shown a η near 0.70. This observations can be explained by the concept of transparency in eq 10. The few-layer Si behaves more like a 2D than bulk material, of which the quantum capacitance C_S remains almost constant when charges are filled into its valence band (VB) or conduction band (CB).⁴ Conversely, when the doping level of graphene is extremely high, its quantum capacitance C_G will be less dependent of the charge density after the van Hove singularity is reached.²⁹ According to eq 10, $\eta = (1 + C_G/C_S)^{-1}$, due to that C_G and C_S are nearly constant, the η value becomes independent of either σ_M or Si doping level. Moreover since C_S is essentially larger than C_G in this case as a result of higher DOS of Si in the VB or CB, it is plausible to have a η larger than 0.5. We also study the charge distribution over the SG interface as a function of σ_M , which exhibits an intriguing profile as shown in Figure 4c. At both positive and negative σ_M regimes, the induced charge density cross section of the system $\Delta\rho_{\text{tot}}$ shows a higher accumulation at the graphene surface than in the Si slab, due to different electronic behaviors of both materials, namely, semimetallic versus semiconducting. A nonlinear pattern is clearly observed throughout the semiconductor slab, as a result the carriers in the Si layer are accumulated in the vicinity of the SG interface. Molecular visualizations of this effect are shown in Figure 4d and 4e for a graphene layer and an intrinsic Si slab. It is found that that most of the orbitals that contribute to the polarization of charge are the $2p_z$ in graphene and $3p_z$ in Si, dependent on the polarity of σ_M applied. According to the results above, we find a good consistency between the macroscopic model and first-principles calculations, which allows us to perform a multiscale analysis for the transparency

of graphene 2DEG to an electric displacement field.

The interesting behavior at the interface has drawn our attention to the possibility of replacing graphene in a MOGS QC structure with other 2D materials. Indeed, as addressed earlier, the ultra-thinness of these materials suggests good potential for 2DEGs. Under the assumption that a 2D material-semiconductor interface satisfies the Schottky-Mott rule, it is suggested that the relation of $\eta = (1 + C_Q/C_S)^{-1}$ still holds (here C_Q substitutes C_G for quantum capacitance in general 2D materials). Since the quantum capacitance can be expressed as $C_Q = g(E)e^2$,³⁴ where $g(E)$ is the DOS at a certain energy level E , we have calculated the DOS as a function of E for a variety of 2D materials^{28,35,36} using the density functional theory (see Supporting Information Figure S2). We also take into account a fractional component of the exact exchange from the Hartree-Fock (HF) theory hybridized with the DFT exchange-correlation functional at the level of the HSE06 hybrid functional³⁷ (see *Methods*). Therefore any limitation of the exchange and correlation functional utilized in the chemical description of the energy levels can be improved. The following 2D materials are considered: transition metal dichalcogenide (TMD) monolayers (MX_2 , $M = \text{Mo, W}$; $X = \text{S, Se, Te}$), silicene (2D allotrope of Si), germanene (2D allotrope of Ge) and phosphorene (monolayer black phosphorus, 2D allotrope of P). The charge density in a 2D material is calculated by integrating the DOS from its intrinsic Fermi level, i.e., $\sigma_{2D} = \int_{E_F}^E g(E')e dE'$. The calculated quantum capacitances for the 2D materials considered as a function of the electron or hole density are shown in Figure 5a and 5c, respectively.

The quantum capacitance of a monolayer 2D semiconductor (TMDs and phosphorene) behaves like a step function and only increases gradually with σ_{2D} , close to that for an ideal 2D semiconductor.⁴ On the other hand, the quantum capacitance of a 2D semimetal, including graphene, silicene, and germanene, exhibits a quadratic relation with respect to σ_{2D} , because they share the same feature of linear $E - k$ dispersion. More importantly, the quantum capacitance for the 2D semimetals are always less than those for the 2D semiconductors under the same charge density. In other words, although there is no states in the band gap,

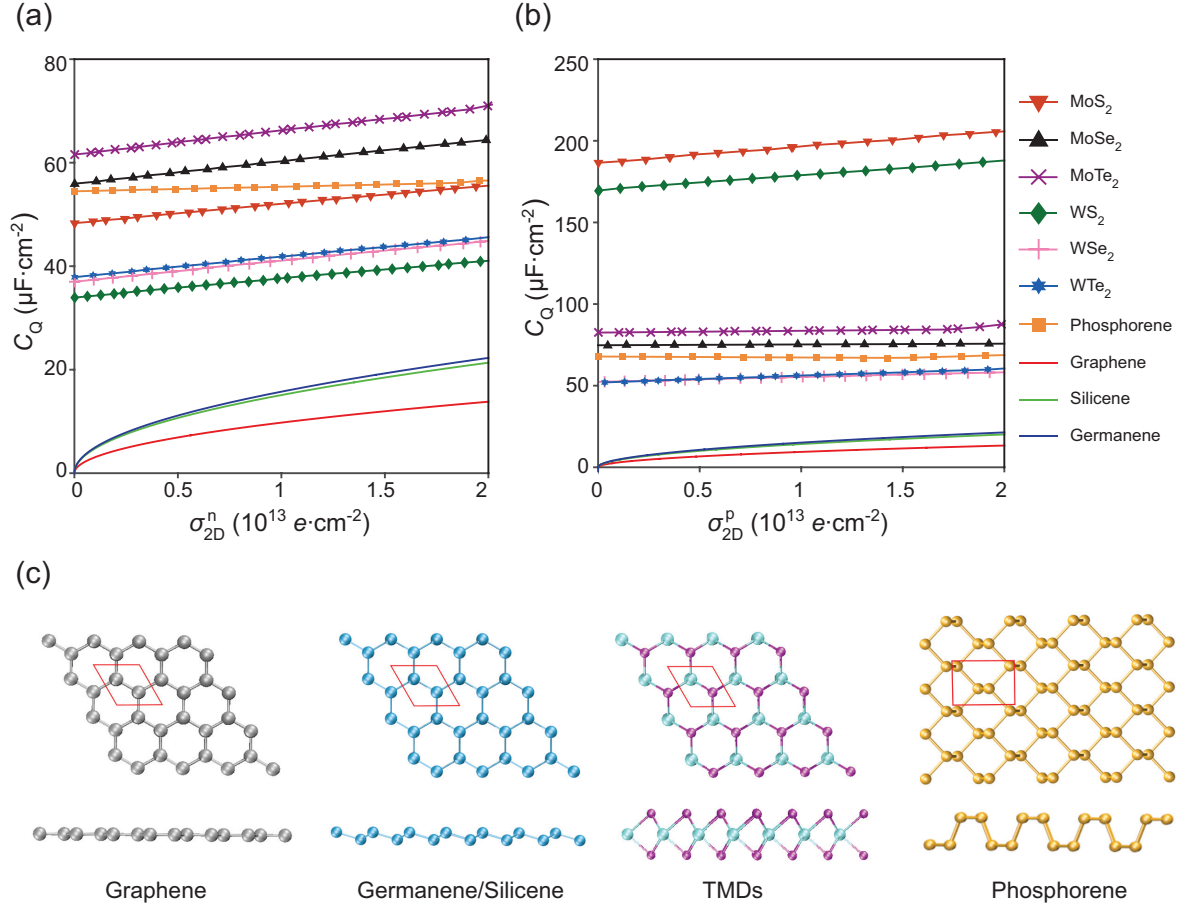


Figure 5: Calculated quantum capacitances (C_Q) for the 2D materials considered, TMDs (MX_2 , $\text{M} = \text{Mo}, \text{W}$; $\text{X} = \text{S}, \text{Se}, \text{Te}$), phosphorene, silicene, germanene and graphene, as a function of the (a) electron density σ_{2D}^n and (b) hole density σ_{2D}^p . (c) Geometries used to calculate the QC using HSE06 hybrid functional for graphene, silicene/germanene, TMDs and phosphorene. The unit cell used in the simulations is highlighted in the panels.

the DOS above the band edge in a 2D semiconductor is significantly higher compared to that in a semimetal, reflecting the fact that the effective mass of carriers in the 2D semiconductors is much larger than that in the 2D semimetals.⁴ This concept also explains why the C_Q for silicene and germanene are similar but higher than that in graphene. Indeed, recent reports have suggested that the Fermi velocities, v_F , in silicene and germanene are only about 60% of that in graphene.^{38,39} combining with eq 10, the observations have led to the conclusion that graphene exhibits the highest transparency to an electric displacement field among all the 2D materials considered here. The theoretical framework also allows us to rank the 2D materials according to their transparency. For example, when the majority carrier is electron, the following rank is predicted: graphene > silicene > germanene > WS₂ > WTe₂ > WSe₂ > MoS₂ > phosphorene > MoSe₂ > MoTe₂. The above analysis for field-effect transparency through multilayer graphene can also be applied to other 2D materials. Indeed, the total DOS of a multilayer 2D material increases with layer number, leading to a higher C_Q and consequently lower field transparency.

Finally, we discuss the effect of the bias V_b between the semiconductor and graphene terminals. Eqs 4 and 5 have suggested that a nonzero V_b changes ψ_0 and σ_S , and in order to satisfy the electroneutrality of the system imposed by eq 1, an adjustment of the graphene's work function ϕ_G occurs, unlike that in a semiconductor-metal (SM) interface. Specifically, Figure 6a illustrates the main differences between SM and SG interfaces. In a semiconductor-metal (SM) junction, the Schottky barrier height ϕ_b remains constant (ϕ_b^0) with V_b , because the work function of metal is independent of its charge density. As a result, the surface potential in the semiconductor layer increases linearly with V_b .¹ On the contrary, in a semiconductor-graphene (SG) junction, under a reverse bias with $V_b > 0$, compare to that with zero bias, one can expect a more negative \mathcal{E}_0 , followed by an increase of σ_S . It is the other way around for $V_b < 0$. As a result, one can expect that σ_G , as well as the resulting ψ_0 and ϕ_b , exhibit a nonlinear dependence on V_b .

Taking a MOGS QC using an n-type silicon ($N_D = 10^{16} \text{ cm}^{-3}$) as an example, the

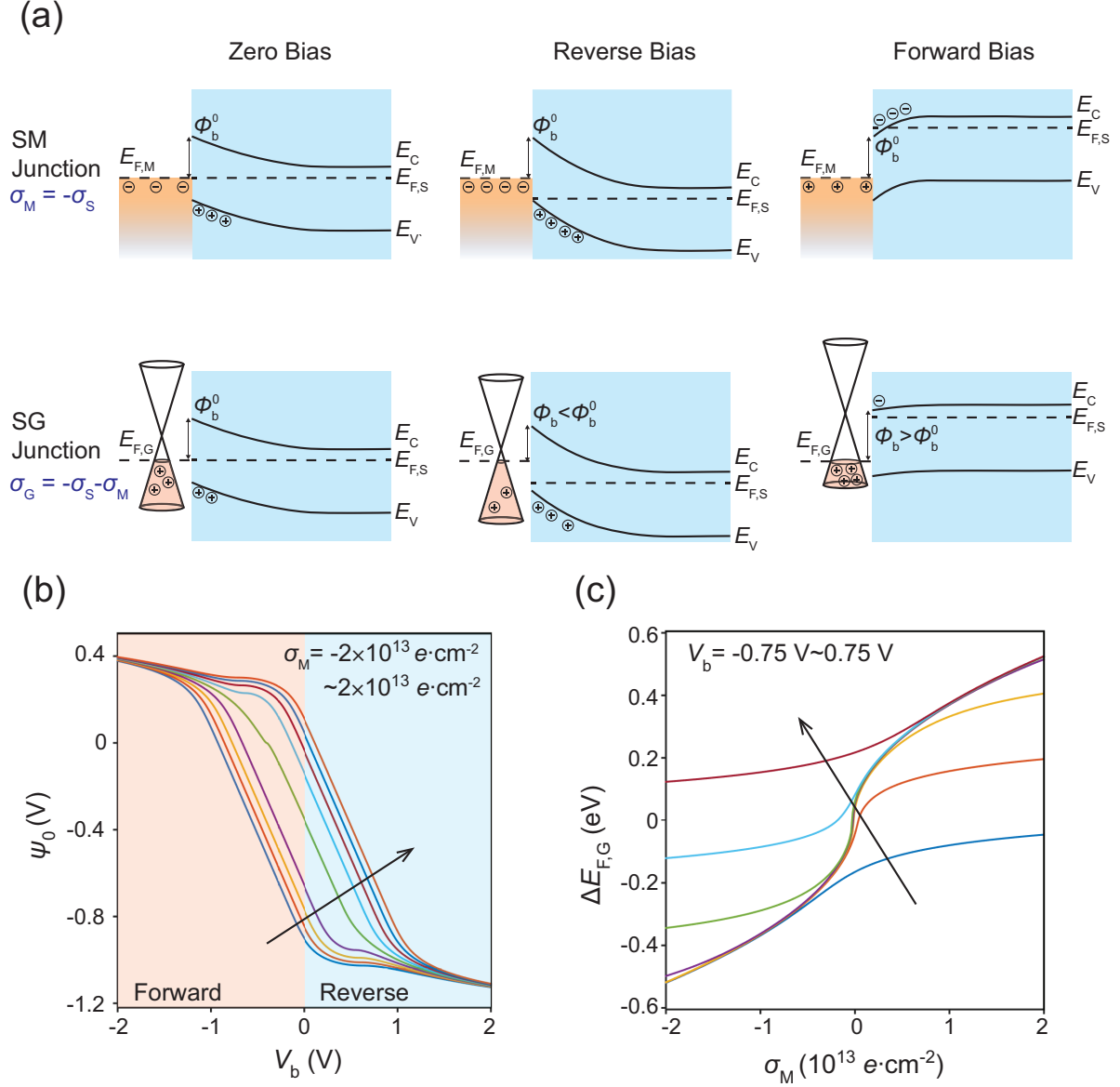


Figure 6: The effect of V_b in a MOGS QC. (a) Schematic illustration of the difference between a semiconductor-metal (SM) and a semiconductor-graphene (SG) junction. (b) Calculated ψ_0 as a function of V_b , under different σ_M values. The arrow indicates the direction of increasing σ_M . (c) Calculated $\Delta E_{F,G}$ as a function of σ_M under different V_b values. The arrow indicates the direction of increasing V_b . A n-type Si with $N_D = 10^{16} \text{ cm}^{-3}$ is considered for (b) and (c).

calculated ψ_0 as a function of V_b under various σ_M values applied is shown in Figure 6b. Compared to the case of $V_b = 0$, in which a relatively wide range of ψ_0 can be tuned by σ_M , it is found that, by increasing $|V_b|$, in both forward and reverse bias regimes, ψ_0 becomes less tunable by σ_M , or in other words, σ_M is losing control over the graphene's Fermi level $E_{F,G}$, when a higher $|V_b|$ is applied. We rationalize this observation by evaluating $E_{F,G}$ with respect to σ_M under constant V_b , or namely, $(\partial E_{F,G}/\partial \sigma_M)_{V_b}$. Using $(\partial \phi_G/\partial \psi_0)_{V_b} = -1$ (see eq 5) and eq 10, it follows:

$$\begin{aligned} \left(\frac{\partial E_{F,G}}{\partial \sigma_M} \right)_{V_b} &= - \left(\frac{\partial \phi_G}{\partial \sigma_M} \right)_{V_b} = \left(\frac{\partial \psi_0}{\partial \sigma_S} \right)_{V_b} \left(\frac{\partial \sigma_S}{\partial \sigma_M} \right)_{V_b} \\ &= \frac{\eta}{C_S} = \frac{1}{C_G + C_S} = \left(\frac{2}{\hbar v_F} \sqrt{\frac{e^3 |\sigma_G|}{\pi}} + \frac{\rho_0}{\mathcal{E}_0} \right)^{-1} \end{aligned} \quad (11)$$

Considering only a slight degree of band bending at $|V_b|=0$, as shown in Figure 6a, when a high forward or reverse $|V_b|$ is applied, an inversion or accumulation layer is formed at the SG interface due to a high degree of band bending, which essentially increases the capacitance of semiconductor C_S . In order to balance the induced σ_S , σ_G also increases, thereby yielding a higher C_G . As suggested by eq 11, a simultaneous rise of C_S and C_G under a high $|V_b|$ results in a significant decrease of $(\partial E_{F,G}/\partial \sigma_M)_{V_b}$, or the tunability of $E_{F,G}$ with respect to σ_M , as shown in Figure 6c. Representative band diagrams of a MOGS QC are shown in Supporting Information Figure S3. This finding is consistent with the experimental observations that the on/off current ratio is lowered by applying a higher drain bias in a graphene-based vertical transistors.^{18–21,40} That is to say, we suggest that the gate-tunable characteristics in a MOGS QC are only observable in a certain $|V_b|$ range. To our knowledge, this effect has not been well discussed in literature.

In conclusion, we have presented the first multiscale approach to understand the penetration of the field effect through a monolayer 2D material in a metal-oxide-2D material-semiconductor quantum capacitor. By using graphene as the model system, first we develop a macroscopic model to describe the charge distribution in graphene and the semiconductor

layers by applying a σ_M on the metal electrode. Depending on the degree of σ_M , the space charge density in the semiconductor layer is modulated in a nonlinear manner, forming an accumulation or inversion layer at the semiconductor/graphene interface, which suggests that graphene is partially “transparent” to an electric displacement field. These results are corroborated by *ab initio* calculations at the level of density functional theory including van der Waals interactions.

We therefore define and formulate the degree of transparency of a monolayer 2D material to an electric displacement field, η , and show that η is determined by the combined effect of graphene quantum capacitance and the semiconductor capacitance. By calculating the quantum capacitance for a variety of 2D materials using hybrid functionals, we predict the ranking for a variety of 2D compounds according to their transparency to an electric displacement field as follows: graphene > silicene > germanene > WS₂ > WTe₂ > WSe₂ > MoS₂ > phosphorene > MoSe₂ > MoTe₂, when the majority carrier is electron. Finally, the effect of the voltage applied between the semiconductor and graphene terminals V_b is discussed. Because a significant increase of the semiconductor capacitance with $|V_b|$ in either reverse or forward bias regime, we find that the gate-tunable characteristics in a MOGS QC are only effective in a certain $|V_b|$ range, which is often ignored in previous reports. We believe that the development of 2D materials-based quantum capacitors and vdW heterostructures will be greatly facilitated by the fundamental principles and theoretical analysis presented here.

Methods

The first-principles simulations reported here are based on density functional theory calculations using the SIESTA method⁴¹ and the VASP code.^{42,43} The generalized gradient approximation⁴⁴ along with non-local van der Waals density functional for the exchange-correlation term⁴⁵ have been used. A double- ζ polarized basis set in SIESTA, and a well-

converged plane-wave cutoff of 400 eV in VASP were utilized in the calculations. Projected augmented wave method (PAW)^{46,47} for the latter, and norm-conserving Troullier-Martins pseudopotentials⁴⁸ for the former, have been used in the description of the bonding environment at the different systems. Atomic coordinates were allowed to relax until the forces on the ions were less than 0.04 eV/Å under the conjugate gradient algorithm. Further relaxations (0.01 eV/Å) do not change appreciably the energetics and geometries. To avoid any interactions between supercells in the non-periodic direction, a 15 Å vacuum space was used in all calculations. In addition to this, a cutoff energy of 150 Ry was used to resolve the real-space grid used to calculate the Hartree and exchange-correlation contribution to the total energy. A basis set of numerical atomic orbitals obtained from the solution of the atomic pseudopotential at slightly excited states as implemented in the SIESTA⁴¹ code was used. We have utilized an energy shift of 50 meV to define the radii of different orbitals. To model the Si surface, we used a periodic array of 4-layer Si(111) slabs, separated by 15 Å thick vacuum space, and terminated by hydrogen atoms at the bottom. Only the two top layers were allowed to relax in contact with graphene, while the rest were kept frozen at Si bulk lattice constant. We have also carried out calculations using screened hybrid functionals at the level of Heyd-Scuseria-Ernzerhof (HSE06) approach.³⁷ In this approximation part of the short range exchange energy is replaced by a portion of exact Hartree-Fock exchange energy. Here we used HSE06 as an example of a hybrid functional because of its successful applications in solids and molecules,^{49–51} and because of its less expensive computational cost to treat the slow-decaying long-range part of the exchange interaction in comparison to the PBE0 functional.⁵² Relevant lattice constants were optimized for each system structure in consideration using PBE and HSE06 methods.

Acknowledgement

T.T. and C.-J.S. are grateful for the financial support from the ETH startup funding. E.J.G.S. acknowledges the use of computational resources from the UK national high performance computing service, ARCHER, for which access was obtained via the UKCP consortium and funded by EPSRC grant ref EP/K013564/1; and the Extreme Science and Engineering Discovery Environment (XSEDE), supported by NSF grants number TG-DMR120049 and TG-DMR150017. The Queen’s Fellow Award through the startup grant number M8407MPH is also acknowledged. P.R. thanks the PhD studentship from the Energy PRP funded by NI-DEL and Queen’s University Belfast.

Supporting Information Available

- Filename: SI.pdf

Additional results for first-principles calculations, representative band diagrams of a MOGS QC, discussion of the influence of interface states on the field-effect transparency and modeling of the field-effect transparency through multilayer graphene.

This material is available free of charge via the Internet at <http://pubs.acs.org/>.

References

- (1) Sze, S. M.; Ng, K. K. *Physics of Semiconductor Devices*; John Wiley & Sons, Inc., 2006.
- (2) Ehrenreich, H.; Spaepen, F. *Solid State Physics*; Academic Press, 2001.
- (3) Luryi, S. *Appl. Phys. Lett.* **1988**, *52*, 501–503.
- (4) Davies, J. H. *The Physics of Low-Dimensional Semiconductors: An Introduction*; Cambridge University Press, 1997.

- (5) Störmer, H.; Dingle, R.; Gossard, A.; Wiegmann, W.; Sturge, M. *Solid State Commun.* **1979**, *29*, 705–709.
- (6) Novoselov, K. S.; Geim, A. K.; Morozov, S. V.; Jiang, D.; Zhang, Y.; Dubonos, S. V.; Grigorieva, I. V.; Firsov, A. A. *Science* **2004**, *306*, 666–669.
- (7) Mayorov, A. S.; Gorbachev, R. V.; Morozov, S. V.; Britnell, L.; Jalil, R.; Ponomarenko, L. A.; Blake, P.; Novoselov, K. S.; Watanabe, K.; Taniguchi, T.; Geim, A. K. *Nano Lett.* **2011**, *11*, 2396–2399.
- (8) Zhang, Y.; Tan, Y.-W.; Stormer, H. L.; Kim, P. *Nature* **2005**, *438*, 201–204.
- (9) Das, A.; Pisana, S.; Chakraborty, B.; Piscanec, S.; Saha, S. K.; Waghmare, U. V.; Novoselov, K. S.; Krishnamurthy, H. R.; Geim, A. K.; Ferrari, A. C.; Sood, A. K. *Nat. Nanotechnol.* **2008**, *3*, 210–215.
- (10) Yu, Y.-J.; Zhao, Y.; Ryu, S.; Brus, L. E.; Kim, K. S.; Kim, P. *Nano Lett.* **2009**, *9*, 3430–3434.
- (11) Aufray, B.; Kara, A.; Vizzini, S.; Oughaddou, H.; Léandri, C.; Ealet, B.; Le Lay, G. *Appl. Phys. Lett.* **2010**, *96*, 183102.
- (12) Dávila, M. E.; Xian, L.; Cahangirov, S.; Rubio, A.; Lay, G. L. *New J. Phys.* **2014**, *16*, 095002.
- (13) Li, L.; Yu, Y.; Ye, G. J.; Ge, Q.; Ou, X.; Wu, H.; Feng, D.; Chen, X. H.; Zhang, Y. *Nat. Nanotechnol.* **2014**, *9*, 372–377.
- (14) Liu, H.; Neal, A. T.; Zhu, Z.; Luo, Z.; Xu, X.; Tománek, D.; Ye, P. D. *ACS Nano* **2014**, *8*, 4033–4041.
- (15) Wang, Q. H.; Kalantar-Zadeh, K.; Kis, A.; Coleman, J. N.; Strano, M. S. *Nat. Nanotechnol.* **2012**, *7*, 699–712.

- (16) Novoselov, K. S.; Fal, V.; Colombo, L.; Gellert, P.; Schwab, M.; Kim, K. *Nature* **2012**, *490*, 192–200.
- (17) Geim, A.; Grigorieva, I. *Nature* **2013**, *499*, 419–425.
- (18) Yang, H.; Heo, J.; Park, S.; Song, H. J.; Seo, D. H.; Byun, K.-E.; Kim, P.; Yoo, I.; Chung, H.-J.; Kim, K. *Science* **2012**, *336*, 1140–1143.
- (19) Yu, W. J.; Li, Z.; Zhou, H.; Chen, Y.; Wang, Y.; Huang, Y.; Duan, X. *Nat. Mater.* **2013**, *12*, 246–252.
- (20) Georgiou, T.; Jalil, R.; Belle, B. D.; Britnell, L.; Gorbachev, R. V.; Morozov, S. V.; Kim, Y.-J.; Gholinia, A.; Haigh, S. J.; Makarovskiy, O.; Eaves, L.; Ponomarenko, L. A.; Geim, A. K.; Novoselov, K. S.; Mishchenko, A. *Nat. Nanotechnol.* **2013**, *8*, 100–103.
- (21) Shih, C.-J.; Pfattner, R.; Chiu, Y.-C.; Liu, N.; Lei, T.; Kong, D.; Kim, Y.; Chou, H.-H.; Bae, W.-G.; Bao, Z. *Nano Lett.* **2015**, *15*, 7587–7595.
- (22) Yu, W. J.; Liu, Y.; Zhou, H.; Yin, A.; Li, Z.; Huang, Y.; Duan, X. *Nat. Nanotechnol.* **2013**, *8*, 952–958.
- (23) Britnell, L.; Ribeiro, R. M.; Eckmann, A.; Jalil, R.; Belle, B. D.; Mishchenko, A.; Kim, Y.-J.; Gorbachev, R. V.; Georgiou, T.; Morozov, S. V.; Grigorenko, A. N.; Geim, A. K.; Casiraghi, C.; Neto, A. H. C.; Novoselov, K. S. *Science* **2013**, *340*, 1311–1314.
- (24) Regan, W.; Byrnes, S.; Gannett, W.; Ergen, O.; Vazquez-Mena, O.; Wang, F.; Zettl, A. *Nano Lett.* **2012**, *12*, 4300–4304.
- (25) Withers, F.; Del Pozo-Zamudio, O.; Mishchenko, A.; Rooney, A. P.; Gholinia, A.; Watanabe, K.; Taniguchi, T.; Haigh, S. J.; Geim, A. K.; Tartakovskii, A. I.; Novoselov, K. S. *Nat. Mater.* **2015**, *14*, 301–306.

- (26) Xu, Y.; He, K. T.; Schmucker, S. W.; Guo, Z.; Koepke, J. C.; Wood, J. D.; Lyding, J. W.; Aluru, N. R. *Nano Lett.* **2011**, *11*, 2735–2742.
- (27) Hill, I. G.; Rajagopal, A.; Kahn, A.; Hu, Y. *Appl. Phys. Lett.* **1998**, *73*, 662–664.
- (28) Xu, H.; Zhang, Z.; Peng, L.-M. *Appl. Phys. Lett.* **2011**, *98*, 133122.
- (29) Das Sarma, S.; Adam, S.; Hwang, E. H.; Rossi, E. *Rev. Mod. Phys.* **2011**, *83*, 407–470.
- (30) Sproul, A. B.; Green, M. A. *J. Appl. Phys.* **1991**, *70*, 846–854.
- (31) Castro Neto, A. H.; Guinea, F.; Peres, N. M. R.; Novoselov, K. S.; Geim, A. K. *Rev. Mod. Phys.* **2009**, *81*, 109–162.
- (32) Nilsson, J.; Castro Neto, A. H.; Guinea, F.; Peres, N. M. R. *Phys. Rev. B* **2008**, *78*, 045405.
- (33) Santos, E. J. G.; Kaxiras, E. *Nano Lett.* **2013**, *13*, 898–902.
- (34) John, D.; Castro, L.; Pulfrey, D. *J. Appl. Phys.* **2004**, *96*, 5180–5184.
- (35) Jiménez, D. *Appl. Phys. Lett.* **2012**, *101*, 243501.
- (36) Nawaz, S.; Tahir, M. *Phys. E* **2016**, *76*, 169–172.
- (37) Heyd, J.; Scuseria, G. E.; Ernzerhof, M. *J. Chem. Phys.* **2006**, *124*, 219906.
- (38) Yan, J.-A.; Stein, R.; Schaefer, D. M.; Wang, X.-Q.; Chou, M. Y. *Phys. Rev. B* **2013**, *88*, 121403.
- (39) Bechstedt, F.; Matthes, L.; Gori, P.; Pulci, O. *Appl. Phys. Lett.* **2012**, *100*, 261906.
- (40) Schwierz, F. *Nat. Nanotechnol.* **2010**, *5*, 487–496.
- (41) Soler, J. M.; Artacho, E.; Gale, J. D.; García, A.; Junquera, J.; Ordejón, P.; Sánchez-Portal, D. *J. Phys. Cond. Matt.* **2002**, *14*, 2745–2779.

- (42) Kresse, G.; Hafner, J. *Phys. Rev. B* **1993**, *48*, 13115–13118.
- (43) Kresse, G.; Furthmüller, J. *Phys. Rev. B* **1996**, *54*, 11169–11186.
- (44) Perdew, J. P.; Burke, K.; Ernzerhof, M. *Phys. Rev. Lett.* **1996**, *77*, 3865–3868.
- (45) Dion, M.; Rydberg, H.; Schröder, E.; Langreth, D. C.; Lundqvist, B. I. *Phys. Rev. Lett.* **2004**, *92*, 246401.
- (46) Blöchl, P. E. *Phys. Rev. B* **1994**, *50*, 17953–17979.
- (47) Kresse, G.; Joubert, D. *Phys. Rev. B* **1999**, *59*, 1758–1775.
- (48) Troullier, N.; Martins, J. L. *Phys. Rev. B* **1991**, *43*, 1993–2006.
- (49) Paier, J.; Marsman, M.; Hummer, K.; Kresse, G.; Gerber, I. C.; Ángyán, J. G. *J. Chem. Phys.* **2006**, *124*, 154709.
- (50) Paier, J.; Marsman, M.; Kresse, G. *J. Chem. Phys.* **2007**, *127*, 024103.
- (51) Franchini, C.; Podloucky, R.; Paier, J.; Marsman, M.; Kresse, G. *Phys. Rev. B* **2007**, *75*, 195128.
- (52) Heyd, J.; Scuseria, G. E.; Ernzerhof, M. *J. Chem. Phys.* **2003**, *118*, 8207–8215.

Graphical TOC Entry

